Extending the Discrete Element Method to Account for Dynamic Confinement and Strain-Rate Effects for Simulating Hard Impacts on Concrete Targets

A. Antoniou, L. Daudeville, P. Marin, S. Potapov

To cite this version:

A. Antoniou, L. Daudeville, P. Marin, S. Potapov. Extending the Discrete Element Method to Account for Dynamic Confinement and Strain-Rate Effects for Simulating Hard Impacts on Concrete Targets. Journal of Dynamic Behavior of Materials, 2024, ⟨10.1007/s40870-024-00438-6⟩. ⟨hal-04667226⟩

HAL Id: hal-04667226
https://hal.science/hal-04667226v1

Extending the discrete element method to account for dynamic confinement and strain-rate effects for simulating hard impacts on concrete targets

Andria Antoniou[1], Laurent Daudeville[1,✉], Philippe Marin[1], Serguei Potapov[2]

Abstract

Concrete plays a pivotal role as a foundational material in critical infrastructure, particularly in nuclear plants. Given the imperative for robustness and safety in such contexts, the design of concrete structures necessitates methodologies capable of precisely predicting damage resulting from impacts. When subjected to impact, concrete experiences high loading rates and significant triaxial stresses in the vicinity of the impacting object, potentially resulting in fragmentation, pore closure and projectile penetration. In addressing these challenges, the discrete element method (DEM) emerges as a suitable approach primarily due to its inherent ability to model discontinuities such as cracking and fragmentation. Within this framework, DEM employing spherical discrete elements (DE) has been implemented into Europlexus, a fast transient dynamics finite element (FE) code. This paper presents a refined constitutive DEM model for concrete, especially accounting for porosity closure under high confinement and the effect of strain-rate on tensile strength and fracture energy. The calibration of constitutive parameters is conducted through the simulations of a series of quasi-static (QS) tests encompassing tension, compression and triaxial compression. The strain-rate dependency parameters are identified through dynamic tensile tests conducted using a split-Hopkinson pressure bar apparatus. The whole constitutive model is presented as well as its calibration. Finally, the validation of the DEM approach is demonstrated through simulations of penetration and perforation tests conducted on concrete targets.

Keywords Discrete element model; Concrete; Compaction; Strain-rate effect; Hard impact test; Perforation

---

[1] Université Grenoble Alpes, CNRS, Grenoble INP, 3SR, 38000 Grenoble, France
[2] IMSIA EDF-CNRS-CEA-ENSTA UMR 9219, 91762 Palaiseau, France
✉ laurent.daudeville@univ-grenoble-alpes.fr

Highlights

- A discrete element model for concrete resulting from several developments is presented in its entirety
- The discrete element model includes tensile brittle damage as well as compaction due to porosity closure
- The parameters of the constitutive model are identified through simulations of quasi-static tests conducted on ordinary concrete under tension, unconfined compression and confined compression
- The strain rate-effect parameters are identified through simulation of split Hopkinson pressure bar tensile tests
- The whole model is validated through the simulation of penetration and perforation tests of plain concrete targets

Introduction

When subjected to intense dynamic loading, such as missile impacts on vital infrastructures, concrete may undergo various degrees of damage, including cracking, spalling, and penetration. Hence, it is crucial to employ reliable design methods that accurately predict concrete behavior during impacts.

In literature, there are comprehensive experimental findings and empirical equations for designing concrete barriers to safeguard nuclear power plants. Riera's approach [1] is suitable for estimating loading in soft impact scenarios, whereas for hard impacts, Petry's formula and its revisions [2-3], along with Berriaud et al.'s formula [4], can be utilized to predict penetration depth and perforation limits, respectively. However, the high expenses associated with full-scale experiments and the limited applicability of empirical equations underscore the necessity for advanced numerical tools. The precision of numerical predictions heavily relies on the accuracy of the constitutive model for concrete materials.

During impact, only a restricted region of a concrete structure experiences high-stress levels that can lead to irreversible compaction. Beyond this region, compression with a moderately triaxial stress level is observed [5-6]. Additionally, near free boundaries, a tensile stress state may occur, resulting in scabbing and spalling [3].

Bischoff et al. [7] conducted an extensive examination of concrete compressive strength sensitivity across a broad spectrum of strain rates, drawing upon experimental data gathered from diverse sources. In scenarios of hard impact, the strain rate can soar to hundreds of s^{-1}.

Malvar et al. [8] collated experimental data from multiple researchers to explore concrete's strain-rate effect in tension. They illustrated the dynamic increase factor (DIF), which signifies the ratio of dynamic to static strength, as a bilinear function of the strain rate, as proposed by the Euro-international committee for concrete (CEB) [9]. This function is divided into moderate and high-rate regimes, with a transitional point around 1 s^{-1}.

In the moderate regime, Rossi et al. [10] attribute this phenomenon to the so-called Stefan effect, construed as an additional resistance arising from pore pressure in the free water. In the high-rate regime, the dependency of concrete's tensile behavior on the loading rate finds its physical explanation in the heterogeneous microstructure of concrete [11]. Increasing the loading rate reduces the microscopic tensile stress near existing cracks and hinders the initiation of new crack formation from initial defects [12].

Fracture energy represents another crucial characteristic of concrete. Schuler et al. [13] delved into its dependency to loading rates by conducting spalling Split-Hopkinson Pressure Bar (SHPB) tests on both notched and unnotched specimens. They demonstrated that at low strain rates, there is no noticeable impact on fracture energy. However, when strain rates exceed approximately 0.3 s^{-1}, there is an increase in fracture energy. Similarly, Weerheijm et al. [12] observed an effect of loading rates on fracture energy, accompanied by a rate-dependent softening curve that shifts towards increased brittleness with higher rates.

Numerical examinations of unconfined compression (UC) experiments [14-17] have highlighted that once strain rates exceed about 1 s^{-1}, the confinement stresses triggered by inertia start to play a notable role, substantially increasing the observed strength during experiments. In other words [18], the compressive strength increase is due to a continuous transition of the stress state from uniaxial stress to uniaxial strain with the loading rate increase.

Piotrowska et al. [19] conducted dynamic tests at strain rates of order of 10^2 s^{-1} and quasi-static (QS) confined compression (CC) tests on concrete, observing that dynamic volumetric stiffness and deviatoric strength values slightly exceeded QS values. Considering the findings from UC and CC tests alongside previous analyses, it can be deduced that the strain-rate effect on concrete in tension is much higher than the effects observed in UC or CC.

A research initiative carried out by the 3SR laboratory at Grenoble Alpes University has aimed to carry out an exhaustive analysis of the triaxial behavior of concrete under high QS confinement pressure. Multiple tests have been conducted on samples made from the same reference concrete with a UC strength of 34 MPa at 28 days [20-21]. The maximum aggregate size (8 mm) was selected in accordance with the specimen size (70 mm diameter and 140 mm length). The experimental campaign has thoroughly investigated the impacts of water/cement ratio, saturation degree, and the effect of coarse aggregate size on concrete behavior under high confinement (up to 650 MPa) [22-25].

To simulate advanced damage states in concrete, Discrete Element Method (DEM) offers advantages due to its discontinuous nature. Unlike Finite Element Method (FEM), DEM is well suited for addressing impact problems as it naturally generates realistic macro-cracks without relying on erosion techniques lacking physical basis. Cundall et al. introduced this method in the early 1980s to model granular media [26-27]. Initially, a limitation of DEM was its challenge in modeling the cohesive behavior of solids. Cusatis et al. [28] proposed an approach where a 3D lattice connects aggregate particles with a distribution determined by the concrete mix design. They define an influence zone for each particle, with forces transmitted through lattice struts. Similarly, Donzé et al. [29], then Hentz et al. [30], used a spring-like model with cohesive interactions between spherical discrete elements (DE), even when not in direct contact, enabling the simulation of cohesive materials like concrete; they defined micro-macro constitutive laws to determine the interactions elastic stiffnesses. While both methods are similar, Cusatis et al.'s approach precisely describes the microstructure of a concrete specimen, albeit being time-consuming due to requiring a large number of particles. In contrast, the higher-scale constitutive behavior modeling of Hentz et al [30] aims to reproduce the macroscopic behavior of concrete for structural engineering applications, enabling the creation of a packing with a reasonable number of DE and lower computational costs. The Hentz et al's nonlinear constitutive model is phenomenological; its parameters are identified through DEM simulations of QS laboratory tests.

Hentz et al.'s [30] concrete model formed the foundation for simulating both soft impacts [31-33] and hard impacts on thin concrete slabs [34]. However, the latter simulations did not involve high mean stress in concrete. In this research, the model developed by Hentz et al. and its subsequent enhancements [31-36] have been integrated, expanding its applicability to encompass impact scenarios featuring elevated mean stress and high strain rates in concrete. This extension integrates a compaction constitutive law to depict porosity closure under high pressure. The strain-rate effect on both tensile strength and fracture energy is determined for the reference concrete. The DIF evolution with strain-rate is bilinear [8-9]. Malvar et al. [8] identified this evolution for ordinary concrete and for low strain rates, while dynamic spalling experiments performed by authors [37] allow identifying the DIF evolution for high strain rates.

The key innovation of this study lies integrating all dissipative nonlinear phenomena and strain-rate effects into a unified DEM model, along with identifying DEM constitutive parameters for ordinary concrete. Some preliminary results were shown in a previous paper [38] but the DEM model was not unified and not calibrated yet.

Section 2 outlines the fundamentals of the DEM model including recent advances. Section 3 details the calibration of DEM parameters through simulations of tests conducted on the reference concrete including QS tension, QS UC, QS CC, and dynamic tensile tests performed with a SHPB device. Section 4 validates this comprehensive approach through simulations of penetration and perforation experiments on thick concrete targets. All the developments were implemented using the Europlexus fast dynamics software [39] co-owned by the CEA (the French alternative energies and atomic energy commission) and the Joint Research Centre of the European Commission.

DEM model for concrete

The utilized DEM is based on a formulation of rigid spherical elements derived from the pioneering work of Cundall et al. to model granular materials [26-27]. Building upon this foundation, Donzé et al. [29] and Hentz et al. [30] extended Cundall et al's formulation to incorporate cohesive interactions, enabling the modeling of materials such as concrete. To create an assembly of spherical DE with different diameters, the open-source SpherePadder++ software [40] is employed. In a first step, the studied concrete specimen geometry is meshed with tetrahedra using the technique developed by Cui et al. [41], then a geometrical process developed by Jerier et al. [42] is applied to generate spheres of varying sizes and to integrate them into the tetrahedral mesh with the maximum compactness.

In the present approach, the spherical DE are not mesoscale components of concrete, such as aggregates, cement paste or voids. Instead, the current model operates at a higher-order scale, aiming to replicate the macroscopic behavior of concrete across both linear and nonlinear regimes. To achieve this, the DE assembly is initially set to be isotropic, which means that the interactions orientations are uniformly distributed in all the directions of the space. This choice mimics the isotropic nature of undamaged concrete and helps avoid the emergence of non-physical cleavage, which can occur when simulating nonlinear concrete behavior using aligned DE or a non-varying distribution of elements sizes [43].

Cohesive and contact interactions

Spherical DE are chosen for their ease of handling interactions between them. The cohesive interaction is initially established between two DE, denoted as *a* and *b*, with radii R_a and R_b, within an interaction range determined by the coefficient λ (Figure 1). D_{ab} represents the distance between the centroids of DE *a* and *b*, with $\lambda > 1$ and $\lambda(R_a + R_b) > D_{ab}$.

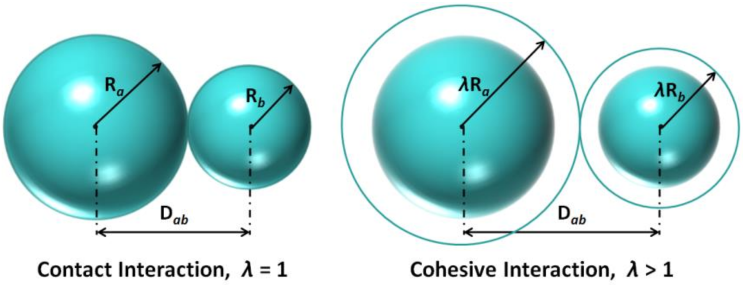

Contact Interaction, $\lambda = 1$ Cohesive Interaction, $\lambda > 1$

Figure 1. The two types of interactions.

This approach enables the definition of an appropriate number of interactions per DE to ensure the isotropic feature of the DE assembly. After breakage, a cohesive interaction may become a new contact interaction if the two DE come in contact (Figure 1). Table 1 outlines all the parameters of the interaction.

Table 1. Physical and geometrical parameters of the interaction between discrete elements *a* and *b.*

Symbol	Parameter	Symbol	Parameter
D_{ab}	Distance between DE *a* and *b* (m)	ξ	Softening parameter (*DIF* = 1)
R_a, R_b	Radii of DE *a* and *b* (m)	ξ_{DIF}	Softening parameter for *DIF*
S_{int}	Interaction surface DE *a* and *b* (m^2)	ξ_{max}	Softening parameter for DIF_{max}
λ	Interaction range coefficient	DIF	Dynamic increase factor
F_N	Normal force between *a* and *b* (N)	DIF_{max}	Maximum dynamic increase factor
F_S	Shear force between *a* and *b* (N)	C_0	Cohesion (Pa)
E	Young’s modulus (Pa)	C_{cel}	Compressive yield stress (Pa)
ν	Poisson ratio	C_{cpl}	Consolidation stress (Pa)
K_N	Normal stiffness (N/m)	Φ_i	Friction angle of cohesive interaction
K_S	Shear stiffness (N/m)	Φ_c	Friction angle of contact interaction
α, β, γ	Micro-macro relations parameters	ξ_1	Hardening coefficient
K_r	Rolling stiffness (Nm)	ξ_2	Consolidated material hardening coef.
β_r	Rolling stiffness parameter	$\dot{\varepsilon}_{st}$	Quasi-static strain rate (s^{-1})
M_{plas}	Yield moment (Nm)	$\dot{\varepsilon}_m$	Moderate strain rate (s^{-1})
η	Yield moment parameter	δ_1	Moderate strain-rate regime slope
D_{init}	Initial distance between DE (m)	δ_2	High strain-rate regime slope
D_{max}	Distance between DE at failure (m)	σ_C	Compressive strength (Pa)

T	Tensile strength (Pa)	σ_{C0}	Reference compressive strength (Pa)
T_{st}	Static tensile strength (Pa)	G_{fD}	Dynamic fracture energy (N/m)
T_{dyn}	Dynamic tensile strength (Pa)	G_{fS}	Static fracture energy (N/m)

Constitutive behavior

Elasticity

The elastic cohesive interaction between DE is modelled through spring-like interactions, with normal and tangential stiffnesses K_N and K_S. The material parameters at the macroscopic scale, namely Young's modulus *E* and Poisson's ratio ν, are directly linked to K_N and K_S through micro-macro relations [29], which are derived from micro-macro relations established for a regular packing of monodisperse spheres [44-45]. Equations (1)-(3) present the micro-macro relations for two elements *a* and *b*, D_{init} is the initial distance between the DE and S_{int} is the interaction surface. *E* and ν are input values, while *α*, *β* and *γ* represent a set of parameters specific to the DE assembly.

$$S_{int} = \pi \ \ min(R_a^2, R_b^2) \tag{1}$$

$$K_N = \frac{E \ \ S_{int}}{D_{init}} \ \frac{1+\alpha}{\beta(1+\nu) + \gamma \ \ (1-\alpha\nu)} \tag{2}$$

$$K_S = K_N \ \ \frac{1-\alpha\nu}{1+\nu} \tag{3}$$

Rolling resistance

When modeling interactions between spherical DE without considering any rolling resistance, the DE assembly displays a brittle behavior, characterized by a shear stiffness lower than the macroscopic stiffness of the material. To address this limitation and better capture the influence of concrete constituents such as cement paste and aggregates, which hinder local rotations, a Moment Transfer Law (MTL) with rolling resistance between DE was introduced by Omar et al. [46].

The link between DE *a* and *b* is conceptualized as a cylindrical beam with a radius $r = min(R_a, R_b)$ (Figure 1). The MTL specifically considers bending rotation (or rolling) and excludes torsion effects. Figure 2 illustrates the assumed elastic perfectly plastic moment-rolling constitutive behavior. The rolling elastic stiffness K_r is defined in Equation (4) where $I = \pi r^4/4$ represents the bending inertia, the factor β_r allows adjusting K_r. The plastic regime is defined with a plateau at the yield moment M_{plas} (Equation

(5)), where T denotes the local tensile strength (Figure 3). Similarly, the factor η allows adjusting the yield moment.

$$K_r = \beta_r \frac{EI}{D_{ab}} \tag{4}$$

$$M_{plas} = \eta \frac{TI}{r} \tag{5}$$

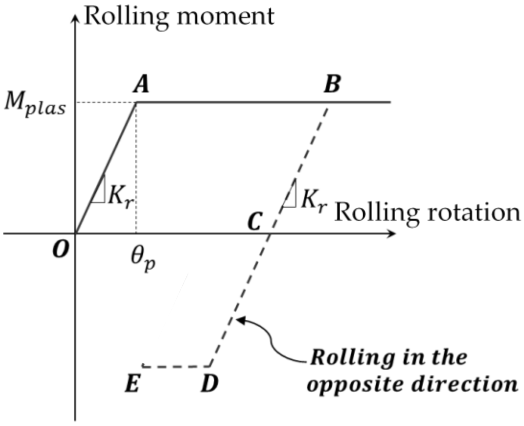

Figure 2. Moment transfer law for rolling resistance [46].

Tensile constitutive behavior

The tensile behavior at the link scale is depicted on the left side of Figure 3 (tensile forces are drawn negative). It is assumed brittle, with no inelastic deformation. The softening behavior occurs when the normal force F_N between the two DE reaches $S_{int}T$, where the stress T is the tensile strength; the softening behavior is defined through the factor ξ. The cohesive interaction between DE is deemed broken once the distance D_{ab} exceeds D_{max}.

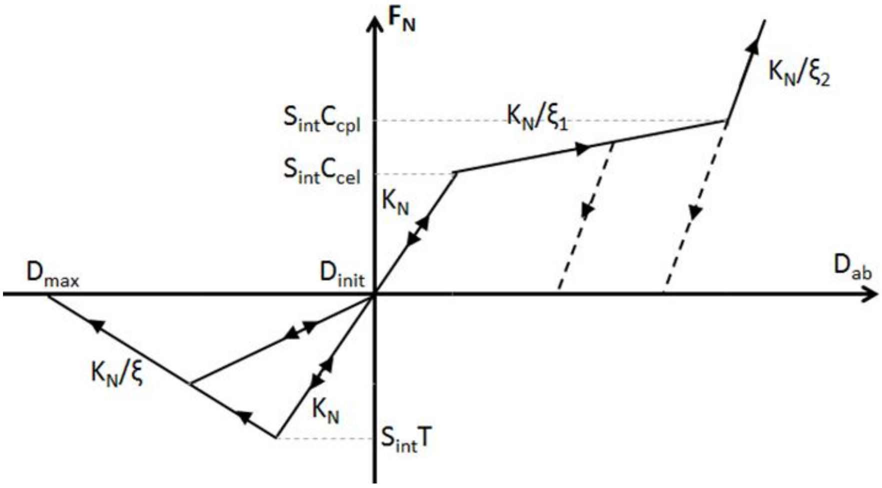

Figure 3. Constitutive model for the normal interaction (left: tensile behavior with damage, right: elastic compression and compaction law).

Failure criterion

The shear behavior and the tensile fracture of the cohesive interaction follow the modified Mohr-Coulomb theory [47]. Two limit function f_1 and f_2, characterizing the nonlinear behavior in shear and tension respectively, are defined in the tangential (F_S) vs normal (F_N) forces plane (Figure 4). The constitutive parameters of the cohesive interaction are the friction angle Φ_i, the cohesion stress C_0, and the tensile cut off stress T ($T = T_{st}$ in case of QS loading).

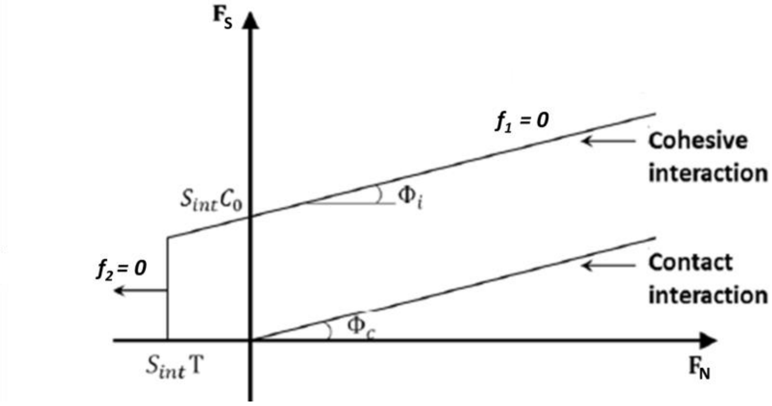

Figure 4. Modified Mohr-Coulomb model (tangential vs normal force).

The yield function f_1 limits the tangential force, thereby capping the maximum shear force, while the function f_2 triggers damage under tension up to the link failure. Upon failure of the cohesive interaction, the two involved DE may re-interact if they come into contact again. In such cases, a contact interaction is established, adhering to a standard Mohr-Coulomb criterion with a contact angle Φ_C. This interaction is limited solely to compression and lacks the ability to exert any tensile force.

Compressive constitutive behavior

Concrete behavior under high mean stress is primarily governed by the compaction phenomenon, stemming from porosity closure [20] [48].

To describe concrete behavior under high mean stresses, Shiu et al. [49] proposed an elasto-plastic with bilinear hardening behavior (right side of Figure 3). In this model, the normal stiffness K_N and the yield strength $S_{int}C_{cel}$ define the elastic behavior. Once the yield strength is surpassed, porosity closure induces hardening (denoted by coefficient ξ_1), resulting in an increase of the elastic stiffness. Complete consolidation of the material is achieved when the compressive force surpasses $S_{int}C_{cpl}$. This signifies that the concrete reaches full compaction, accompanied by additional stiffness enhancement through the hardening coefficient ξ_2.

Shiu et al.'s model was implemented into Europlexus. However, it is important to note that the present model does not consider the influence of the water saturation ratio in the constitutive behavior. In a recent development, Benniou et al. [50] incorporated the influence of saturation ratio in a DEM model of concrete. However, numerical simulations were limited to laboratory tests of wet concrete specimens under confined compression conducted by Vu et al. [23] and by Accary et al. [51]. In the latter tests, the authors could measure the interstitial pore pressure.

Strain rate effect in tension

It is important to highlight that the rate dependency of concrete in tension stems from the inherent heterogeneity within its microstructure [11-12]. Consequently, modeling concrete at the macro-scale necessitates the consideration of strain rate effects in tension. During UC and CC tests, the observed strength enhancement recorded during SHPB experiments is notably lower [14-17], it is attributed to the influence of radial inertia forces [14].

In the current DEM approach, strain-rate sensitivity at the scale of DE is considered primarily in tension. The DIF, representing the ratio of dynamic to QS strengths (T_{dyn}/T_{st}), evolves with strain rate. Drawing inspiration by the CEB formula [9], this evolution follows two distinct regimes as described by Equation (6).

$$DIF = \frac{T_{dyn}}{T_{st}} = \begin{cases} 1 & \dot{\varepsilon} \leq \dot{\varepsilon}_{st} \\ \left(\frac{\dot{\varepsilon}}{\dot{\varepsilon}_{st}}\right)^{\delta 1} & \dot{\varepsilon}_{st} < \varepsilon^{\cdot} \ \leq \dot{\varepsilon}_m \\ \theta\left(\frac{\dot{\varepsilon}}{\dot{\varepsilon}_{st}}\right)^{\delta 2} & \dot{\varepsilon} > \dot{\varepsilon}_m \end{cases} \quad with \quad \delta_1 = \frac{1}{1 + 8\frac{\sigma_C}{\sigma_{C0}}} \ ; \theta = \left(\frac{\dot{\varepsilon}_m}{\dot{\varepsilon}_{st}}\right)^{(\delta 1 - \delta 2)} \tag{6}$$

$\dot{\varepsilon}_{st}$ and $\dot{\varepsilon}_m$ are the quasi-static and moderate strain rates, δ_1 and δ_2 are the slopes of the first and second regimes. σ_C stands for the QS compressive strength of concrete, and $\sigma_{C0} =$ 10 MPa is a reference value.

The first regime is influenced by the QS compressive strength of concrete σ_C. Notably, the increase in tensile strength is more prominent for concretes with lower compressive strengths. The transition to the second regime occurs at $\dot{\varepsilon}_m$, signifying a shift to high strain-rate dependency characterized by a sharper slope δ_2.

Erzar et al. [52] demonstrated that the shear response of concrete exhibits strain-rate dependency, albeit significantly lower than in tension. The corresponding DIF in shear is arbitrary capped at a value of 2.0. Utilizing the modified Mohr-Coulomb criterion (Figure 4), the maximum dynamic increase factor DIF_{max} can be determined using Equation (7).

$$DIF_{max} = \frac{2.0 \ \ C_0}{tan(\varphi_i)T_{st}} \tag{7}$$

Weerheijm [12] and Schuler et al. [13] observed a slight increase of fracture energy in the high strain-rate regime and a post-peak slope that increases with the strain rate. Schuler et al. evaluated the dynamic intensification factor for fracture energy $\frac{G_{fD}}{G_{fs}}$ between 2 and 3 for highest tested strain rates.

Figure 5 illustrates the proposed modeling of the strain-rate effect in tension accounting for the tensile strength enhancement and the slight increase of the fracture energy. These evolutions correspond to Equations (7)-(11). The parameter ξ_{max} that governs the fracture energy at the strain rate corresponding to the maximum dynamic increase factor DIF_{max} can be determined through Equation (8) with the maximum dynamic intensification factor for fracture energy evaluated by Schuler et al. [13].

This simple choice of DIF evolution facilitates a straightforward identification of parameters through the simulation of dynamical tensile tests.

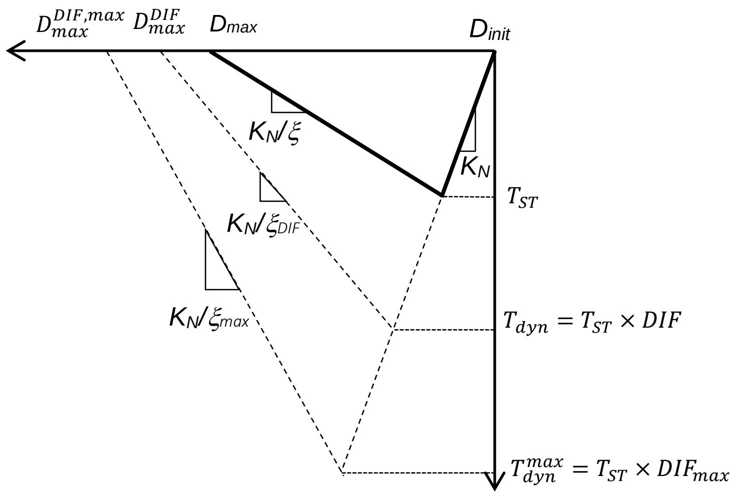

Figure 5. Tensile constitutive behavior of concrete considering the strain rate influence.

$$\frac{G_{fD}}{G_{fS}} = \frac{DIF^2(1+\xi_{max})}{1+\xi} \tag{8}$$

$$K_N/_{\xi_{DIF}} = K_N/_{\xi} + \left(K_N/_{\xi_{max}} - K_N/_{\xi}\right)\left(\frac{DIF-1}{DIF_{max}-1}\right) \tag{9}$$

$$\frac{1}{\xi_{DIF}} = \frac{1}{\xi} + \left(\frac{1}{\xi_{max}} - \frac{1}{\xi}\right)\left(\frac{DIF-\ 1}{DIF_{max}-1}\right) \tag{10}$$

$$\frac{D_{max}^{DIF}}{D_{max}} = \frac{DIF(1+\xi_{DIF})}{1+\xi} \tag{11}$$

Constitutive behavior parameters identification

The identification of the DEM constitutive parameters for concrete relies on the following equations and figures:

- Elastic behavior: micro-macro relations (1)-(3), parameters α, β and γ.
- Quasi-static uniaxial nonlinear constitutive behavior: Equations (4)-(5), Figure 3 and Figure 4, parameters β_r, η, T_{st}, ξ, C_0, Φ_i and Φ_c.
- Quasi-static triaxial compaction behavior: Figure 3, parameters C_{cel}, C_{cpl}, ξ_1 and ξ_2.
- Tensile strain-rate dependency: Equations (6)-(11), parameters $\dot{\varepsilon}_{st}$, $\dot{\varepsilon}_m$, δ_1, δ_2 and ξ_{max}.

The identification procedure of these parameters is detailed in Antoniou's doctoral dissertation [37]. It relies on a few simulations of laboratory tests.

Influence of discrete element discretization on elastic properties of a discrete element assembly

A geometrical method developed by Jerier et al. [42] is utilized to generate the DE assembly. This algorithm generates spheres of varying sizes and embeds them into a tetrahedral FE mesh. As mentioned previously, the parameters α, β and γ in the micro-macro relations (2)-(3) are dependent on the packing of spherical DE. The interaction coefficient λ allows adjusting the number of interactions (Figure 1). Rousseau et al. [33] selected an average number of 12 links per DE. This empirical choice allows identifying λ, combined with the appropriate packing technique; it ensures the isotropy of the DE assembly. The average number of 12 links per DE is a fixed parameter for all the numerical simulations presented in this paper.

In a previous study [36], the authors demonstrated that for a given set of parameters such as the average number of interactions per DE (set at 12), the ratio of DE radii R_{max}/R_{min}, the ratio of average DE radius over average FE size, and a random distribution of DE sizes, the generated homogeneous DE assembly has elastic properties that are very minimally affected by discretization.

Figure 6 depicts the various samples employed to simulate QS UC tests of rectangular parallelepiped with a square cross-section and a length to edge sizes ratio of 2. For all DE meshes, the following ratios were used: R_{max}/R_{min} = 3 and FE tetrahedron edge/DE mean diameter = 4. The number of DE ranges from 122 to 77556. The parameters α, β and γ in the micro-macro relations (2)-(3) were identified using sample 4, which was derived from the tetrahedral mesh containing 4 tetrahedra per transverse edge. These parameters were determined along with the macroscopic elastic parameters E (35 GPa) and ν (0.2).

The values α = 3.9, β = 3.75 and γ = 5 are optimal parameters for replicating the macroscopic linear elastic behavior.

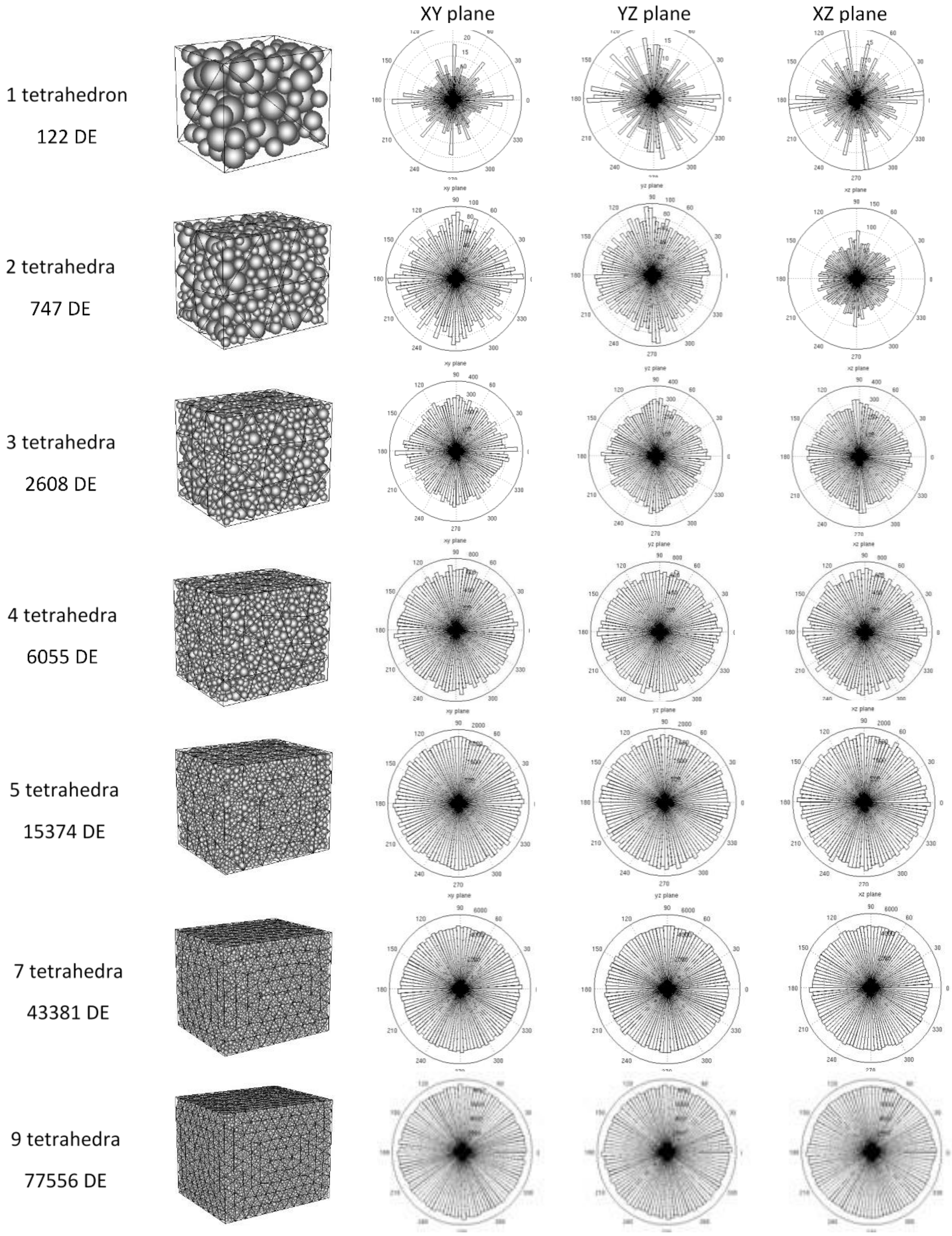

Figure 6. DE sample meshes with the number of tetrahedral per edge and distribution of interactions orientations in the XY, YZ and XZ planes [36].

After identifying α, β and γ parameters, Figure 7 illustrates the evolution of numerically measured macro properties E and ν through simulations of QS UC tests performed on samples with various discretizations. The measured macro properties significantly deviate from the targeted values (E = 35 GPa and $\nu = 0.2$) only for the coarsest discretization (1 tetrahedron per transverse edge). This result demonstrates that for a non-coarse discretization using a set of parameters close to those utilized for identifying α, β and γ, the elastic macro properties E and ν of the generated DE medium will be close to the targeted macro properties used in Equations (2)-(3).

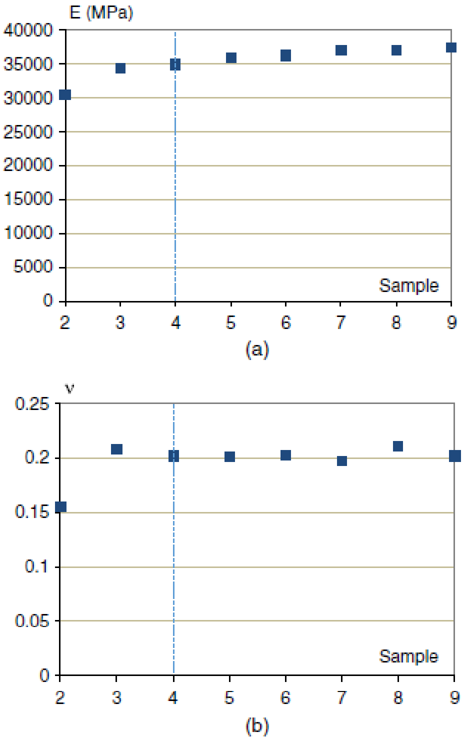

Figure 7. Reproducibility of (a) Young's modulus and (b) Poisson's ratio [36].

Reference concrete properties

The last section will present the validation of the DEM approach for predicting damage in thick concrete targets under hard impact. The targets are made of R30A7 concrete (Table 2). They were cast and submerged in water until the date of the test to get specimens with well-controlled material properties. Therefore, the tested concrete can be considered fully saturated with water.

The constitutive parameters of the DEM model are calibrated to replicate the macroscopic behavior of the reference ordinary fully saturated concrete R30A7, extensively studied in both QS and dynamic conditions at the 3SR laboratory of the University Grenoble Alpes. High-quality cement is used to ensure good reproducibility for a material with low cement volume. R30A7 concrete contains siliceous rolled aggregates with a maximum size of 8 mm obtained from natural deposits (99% quartzite). Table 2 provides the composition and mechanical properties of R30A7 concrete. The compressive strength of R30A7 concrete at 28 days of ageing is 34 MPa. The saturated concrete samples are held in water for about 4 months before testing [21].

Table 2. Composition and mechanical properties of reference ordinary concrete R30A7 [20-21].

Composition		**Mechanical properties**	
Cement CEM I 52.5N	263 kg/m^3	Compressive strength	34 MPa
Sand D_{max} 1.8 mm	838 kg/m^3	Tensile strength	3.6 MPa
Gravel 0.5-8 mm	1008 kg/m^3	Porosity accessible to water	12 %
Water	169 kg/m^3	Slump	7 cm
W/C ratio	0.64	Density	2278 kg/m^3
		Young’s modulus	25 GPa
		Poisson’s ratio	0.16

Quasi-static uniaxial behavior parameters

The identification of DEM uniaxial behavior parameters is conducted through simulations of tension and UC tests. To simplify the generation of the DE assembly, the numerical sample is a rectangular parallelepiped with a square cross-section and a length to edge sizes ratio of 2 (sample 4 of Figure 6), while experimental specimens are cylinders with a circular base.

Parameters β_r and η of the MTL (Figure 2) are calibrated thanks to the experimental stress-strain curve of a UC test. The correct replication of the peak stress and the curve shape allows identifying $\beta_r = 5$ and $\eta = 5$. It is noteworthy that η has no influence on the linear elastic behavior and β_r a very slight one [35]. Consequently, these parameters have no influence on the previously identified parameters α, β and γ.

The tensile cut off stress T_{st} significantly affects the tensile and UC strength values of concrete. However, the softening factor ξ has minimal effect on the post-peak shape of the stress-strain curve in compression; instead, it alters the ultimate tensile strain. Parameters such as cohesion stress C_0 and friction angles Φ_i and Φ_c do not directly influence the tensile behavior of concrete. However, C_0 affects the compressive peak stress, while the two friction angles have a slight impact on the post-peak regime. Following an examination of each parameter's influence on macroscopic behavior in uniaxial tension and compression [37], constitutive parameters governing QS nonlinear behavior were determined for

R30A7 saturated concrete. The identified values are as follows: T_{st} = 2.5 MPa, ξ = 3, C_0 = 4.5 MPa, $\Phi_i = \Phi_c$ = 20°.

Quasi-static triaxial behavior parameters

The constitutive parameters of the compaction law (Figure 3) are determined through simulations of hydrostatic and oedometric tests conducted on fully saturated concrete specimens at high confining pressure using the high-capacity triaxial press Giga (Figure 8). In a hydrostatic test, isotropic pressure is applied uniformly around the entire specimen, increasing linearly with time. On the other hand, an oedometric test restrains radial deformation while the specimen is axially compressed. These tests allow for the characterization of concrete behavior under high confinement conditions.

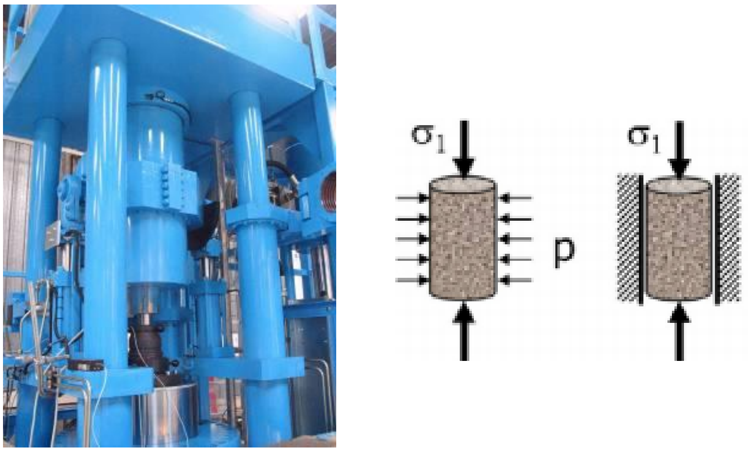

Figure 8. High capacity triaxial press Giga [21] and performed tests (hydrostatic σ_1= p).

To simulate triaxial compression tests, the DE assembly is generated with the same discretization parameters as those defined by Potapov et al. [36] for the simulation of UC and tension tests. This approach ensures consistency in representing the material behavior across various loading conditions.

Similar to uniaxial tests simulations, numerical samples for hydrostatic and oedometric tests have a square base, while experimental specimens have a circular one. They are represented by 0.1x0.1x0.1 m^3 cubes.

The polydisperse assembly consists of 4427 DE with a maximum radius of 5.4 mm, a minimum radius of 1.8 mm, and a compactness of 0.59. In the simulation, six rigid planes exert contact forces on each face of the cube, replicating the loading conditions of the hydrostatic and oedometric tests.

The parameters identified by comparison with experimental results (Figure 9) are ξ_1 = 1.5, ξ_2 = 0.3, C_{cel} = 50 MPa and C_{cpl} = 300 MPa.

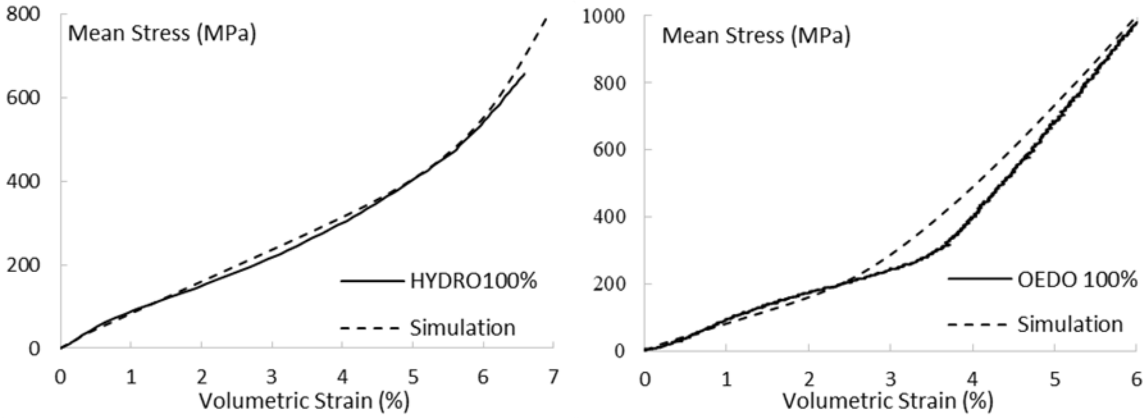

Figure 9. Simulation of hydrostatic (left) and oedometric (right) tests.

Strain-rate dependency parameters

This subsection focuses on the identification of constitutive parameters for Equations (6)-(11) for R30A7 saturated concrete.

The parameter ξ_{max} at the strain rate corresponding to the maximum dynamic increase factor DIF_{max} is determined through Equation (8) and the maximum DIF for fracture energy evaluated by Schuler et al. [13] ($\frac{G_{fD}}{G_{fS}} = 2.56$). The identification gives $\xi_{max} = 2.56\ 10^{-2}$.

Malvar et al. [8] identified the material parameters of the first regime for ordinary concrete (Equation (6)). The QS strain rate of the first regime is $\dot{\varepsilon}_{st} = 10^{-6}$ s^{-1} and the slope of this regime is $\delta_1 = 0.0355$ for $\sigma_C =$ 34 MPa.

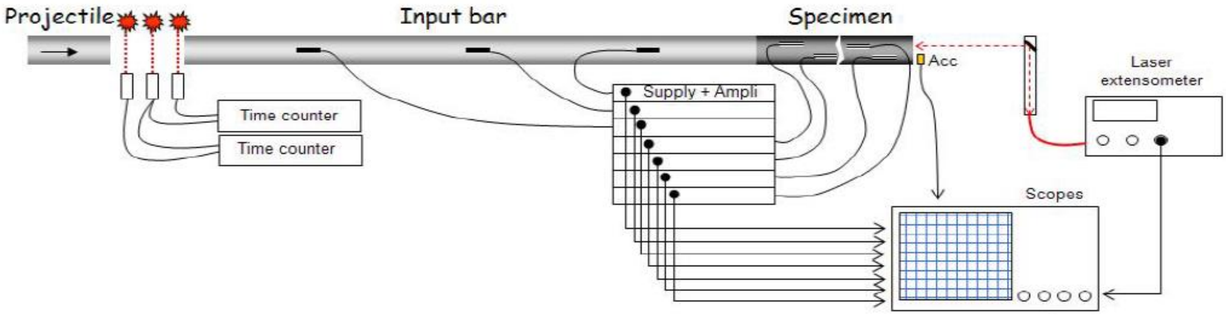

Figure 10. Spalling SHPB experimental setup [54].

The identification of the second high strain-rate regime is carried out through simulations of spalling tests using a SHPB device (Figure 10). Antoniou [37] conducted spalling tests at strain rates 30 s^{-1} and 50 s^{-1} on two fully saturated R30A7 specimens. In these tests, the specimen is subjected to a compression pulse that is reflected as a tensile wave. When the amplitude of the reflected wave exceeds that of the transmitted one, a dynamic tensile stress develops in the specimen, potentially leading to its fracture. The pullback velocity, that is the difference between the maximum velocity and the first rebound velocity observed on the rear face, is correlated with the dynamic tensile strength of concrete [53].

The same procedure [36] is employed to generate the DE packing for the DEM simulation of the dynamic spalling test. The specimen is cylindrical with a diameter of 46 mm and a length of 142 mm. It comprises 18376 DE with a maximum radius of 2.1 mm, a minimum radius of 0.7 mm, and a compactness of 0.59 (Figure 11).

In the simulation, a compressive pulse is directly applied to the front face of the sample, while the particle velocity of the rear face is measured to identify the evolution of DIF parameters with the strain rate. The number of broken links of a DE divided by its total number of initial links defines the damage indicator for the considered DE. Figure 11 shows that at 30 s^{-1}, the specimen is split into two parts of approximatively the same size.

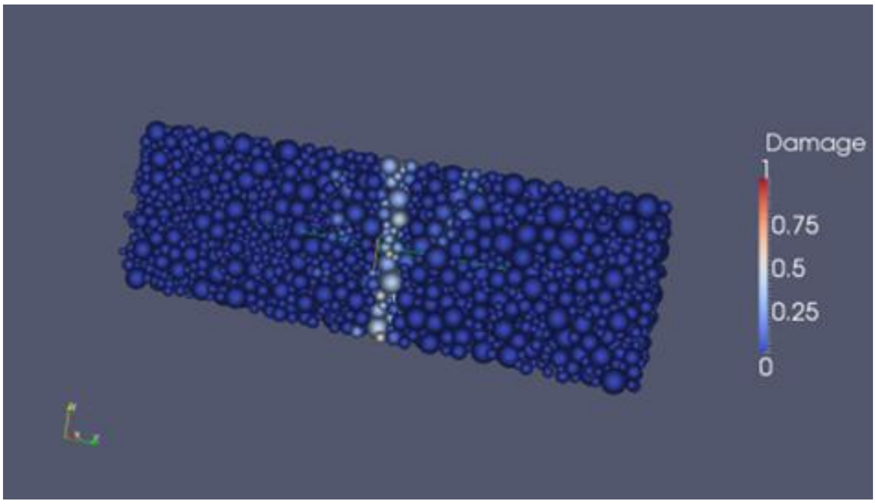

Figure 11. DE model of the specimen tested at 30 s^{-1} and damage at the end of the test.

$\dot{\varepsilon}_m$ and δ_2 (Equation (6)) are the constitutive parameters of the second regime of the DIF evolution. They are determined through simulation of two spalling tests. The proper capture of the peak and rebound velocity observed on the rear face validates the parameters identification (Figure 12). With $\delta_2 = 0.333$ and $\dot{\varepsilon}_m = 1$ s^{-1}, the simulation yields the closest match to the experimental results.

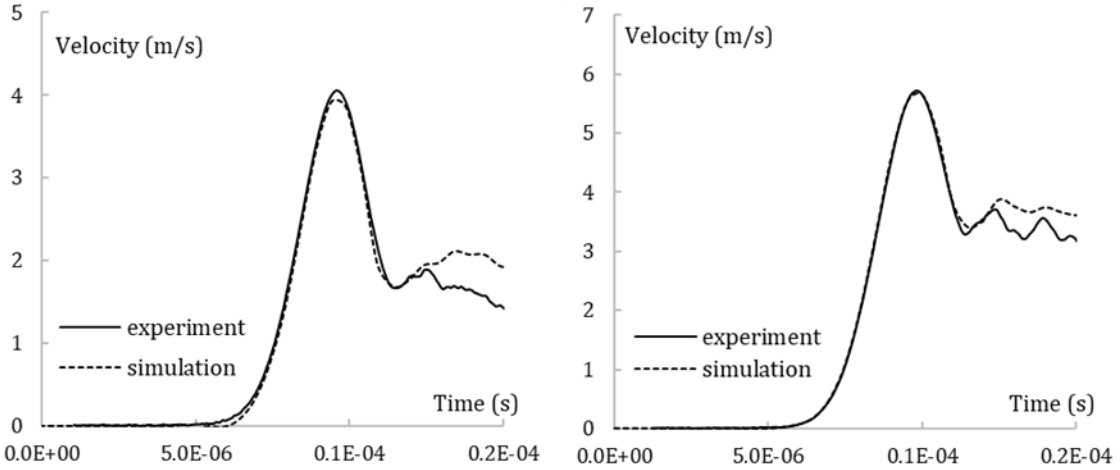

Figure 12. Experimental and numerical rear face velocity of the spalling test at 30 s^{-1} (left) and 50 s^{-1} (right).

Figure 12 compares the numerical simulations with the experimental data. The curve obtained in the simulation closely replicates the slope of the rising velocity pulse of the rear face. Additionally, the simulation adequately predicts the peak and first rebound velocities. These results confirm the reliability of the proposed DIF constitutive behavior for concrete within the tested range of strain rates.

However, it is essential to investigate the ability of the DEM model to reproduce the behavior of concrete under higher strain rates. Erzar et al. [52] utilized the spalling technique to investigate the response of saturated R30A7 concrete across a broad range of strain rates. The dynamic strength, evaluated using Equation (6) and the identified values for $\dot{\varepsilon}_m$ and δ_2, is compared with experimental measurements (Figure 13). Spalling test data from Erzar et al. [52] are represented by dots, while the numerical results are depicted with a dashed line. The correct comparison validates the proposed DIF evolution with strain rate.

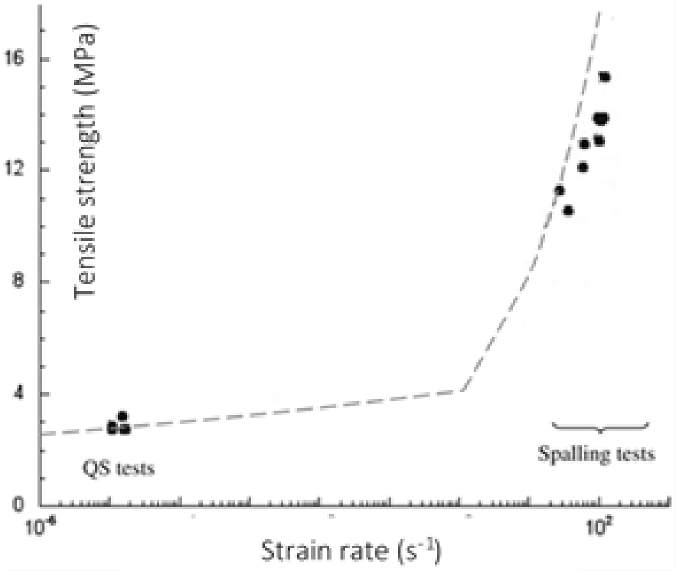

Figure 13. Tensile strength of saturated R30A7 concrete [52] and DEM model predictions.

Validation of the DEM approach through the simulation of penetration and perforation tests

After identifying constitutive parameters of the DEM model, the entire DEM approach is validated through the simulation of hard impact tests conducted by CEA on thick saturated R30A7 concrete targets [55]. These simulations are particularly relevant because they involve both tensile damage at high strain rates and compaction due to high triaxial stresses, which are characteristic phenomena in these tests.

Presentation of tests

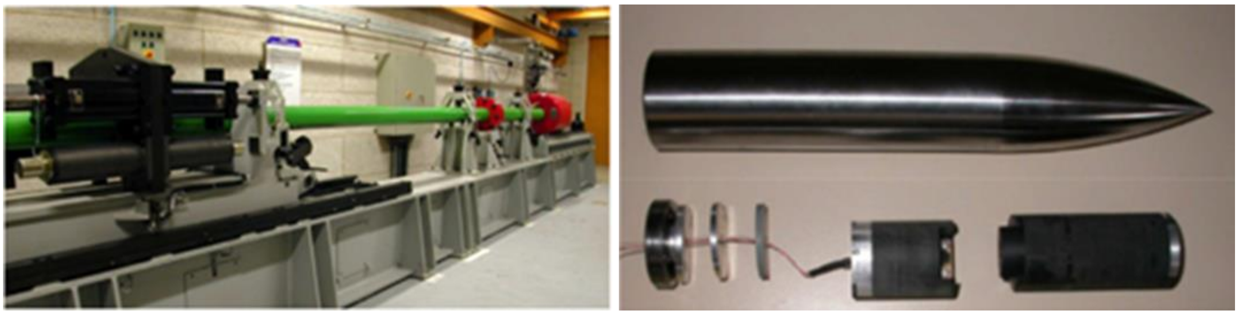

Figure 14. Gas launcher and projectile with its accelerometer [55].

A gas device (Figure 14, left) is employed to launch ogive-nosed projectiles made of 35NCD16 steel. These projectiles have a nose radius to diameter ratio of 5.77, a shank diameter of 52 mm, a length of 299 mm and a mass of 2.442 kg (Figure 14, right).

The targets used in the experiments have a 800 mm diameter. They consist in three 15 mm thick steel jackets filled with plain R30A7 concrete. They were stored 149 days in water and immediately tested, therefore concrete can be considered saturated with water. One perforation test was conducted on a target with a thickness (H) of 300 mm, with a striking velocity of 333 m/s (Figure 15, left). Additionally, two penetration tests were performed on targets with a thickness (H) of 800 mm: one at low velocity (227 m/s) and the other one at high velocity (347 m/s) (Figure 15, right).

An accelerometer in the steel projectile (Figure 14, right) allowed recording the axial deceleration during the experiment. The dimensions and shapes of ejected concrete in the rear and front faces of the targets were measured with a topographic laser system.

Figure 15. Post test images of the perforation concrete target (left, H = 300 mm) and the penetration concrete target (right, H = 800 mm).

Simulation of tests

In the Europlexus simulation, concrete cylinder is modeled with DE. The steel elements, that are the confining jacket and the projectile, are modeled with tetrahedral FE with a linear elastic behavior (Figure 16). Table 3 provides information on the number of DE, as well as the maximum and minimum radii and compactness of the perforation and penetration concrete DE assemblies.

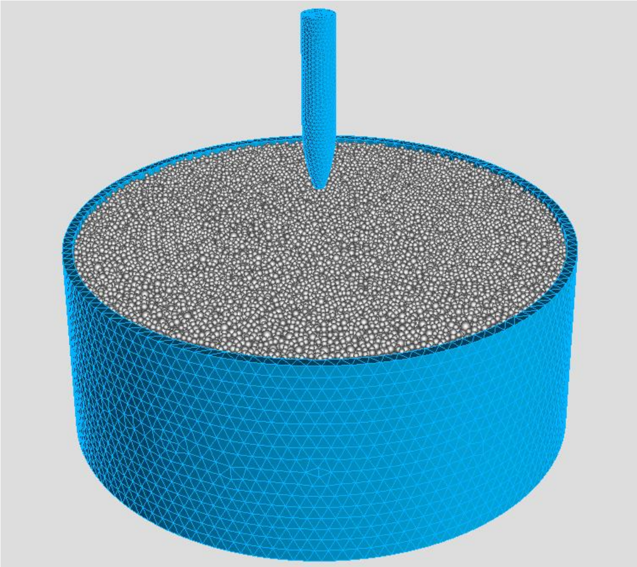

Figure 16. Perforation test model with DE concrete specimen confined with FE steel jacket and impacted by a FE steel projectile

Table 3. Features of perforation and penetration DE models.

	Number of DE	R_{max}	R_{min}	Compactness
Perforation	141765	0.9	0.3	0.61
Penetration	336467	0.94	0.31	0.62

Figure 17 shows the excellent agreement between the calculated and measured axial displacements of the projectile. Additionally, Figure 18 displays a cross-sectional view of damage state of the concrete target and the projectile, 2.5 ms after the impact on the front face of the target. It is worth noting that despite the symmetrical nature of the target specimen, the projectile does not follow a rectilinear trajectory due to the randomly and non-symmetrical distribution of spherical DE.

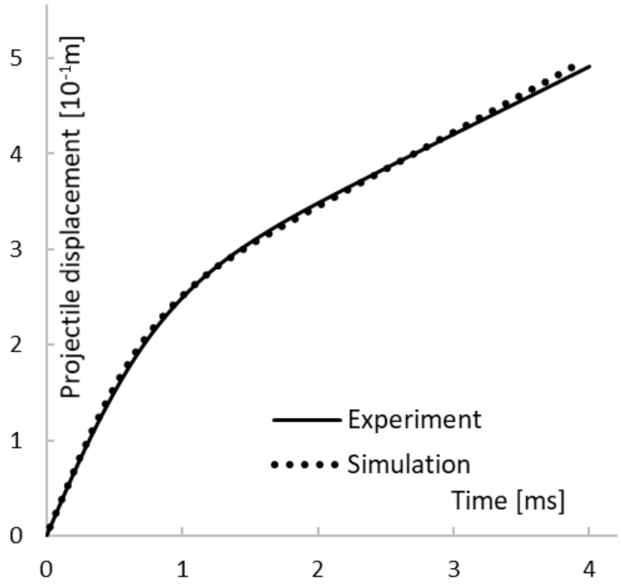

Figure 17. Perforation test, simulation and experiment, projectile axial displacement.

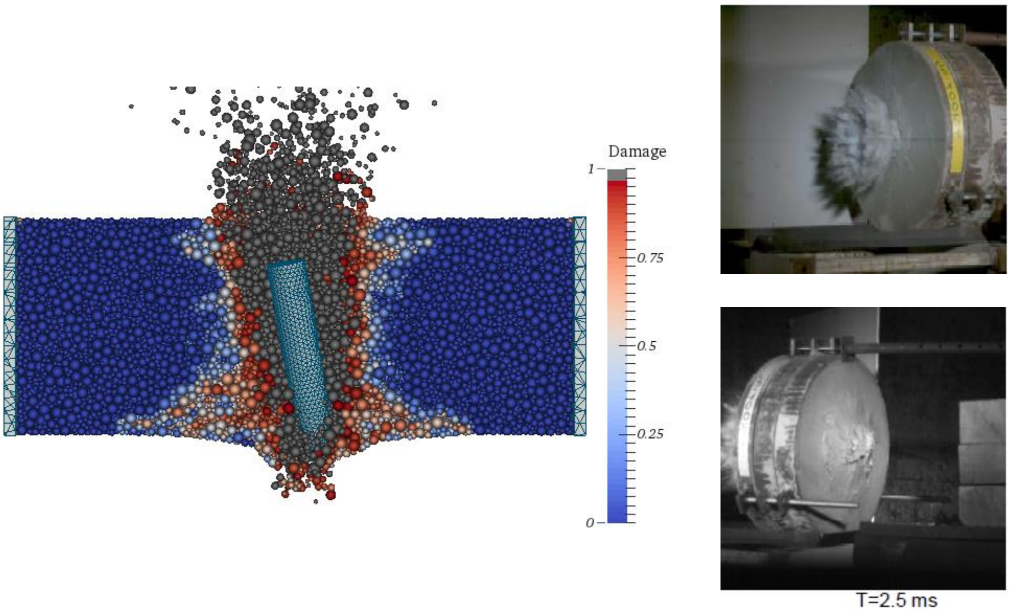

Figure 18. Perforation test after 2.5 ms: damage state of concrete and views of the front and rear faces of the target.

Figure 19 shows the zones of ejected concrete after the perforation test and the numerical damage pattern. During the simulation, an initial cratering phase was observed, followed the initiation of spalling, and then the tunneling phase due to penetration of the projectile. Subsequently, scabbing appeared at the rear face, and finally, the projectile perforated the target [37]. The damage pattern generated by the DEM model appears to be in good accordance with the experimental observations, with more pronounced diagonal cracks observed at the bottom of the perforated specimen compared to the top.

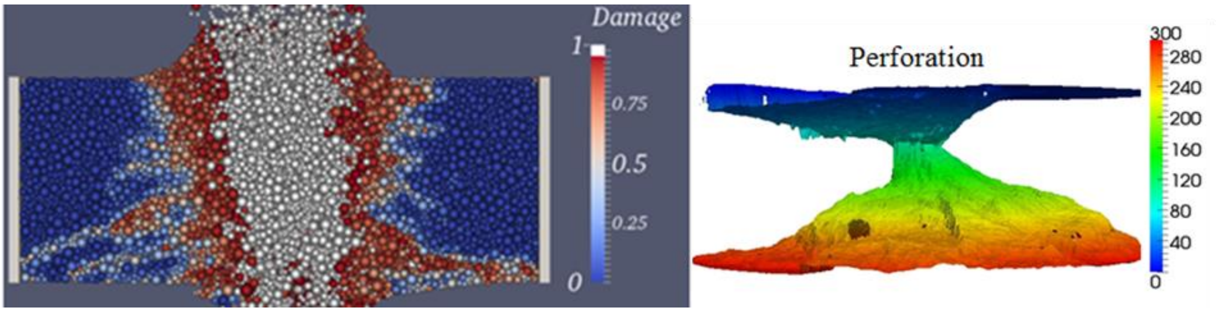

Figure 19. Perforation crack pattern: simulation and experiment.

Figure 20 illustrates the axial displacement of the projectile during the penetration test at 227 m/s. The simulation closely predicts the penetration depth but the time evolution is slightly different, especially at the end of the test.

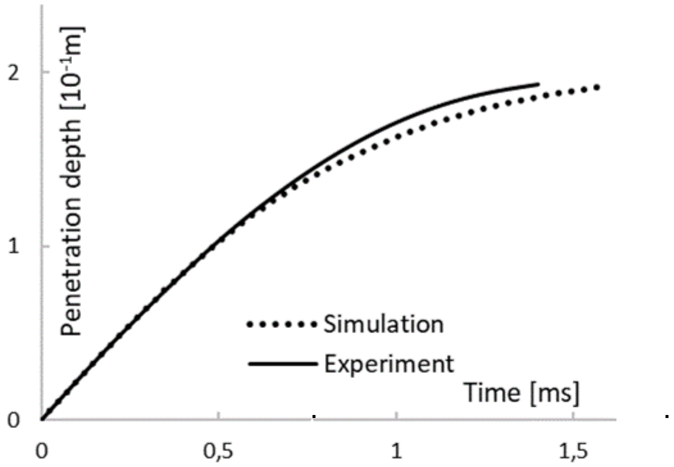

Figure 20. Penetration test at 227 m/s, simulation and experiment, projectile axial displacement

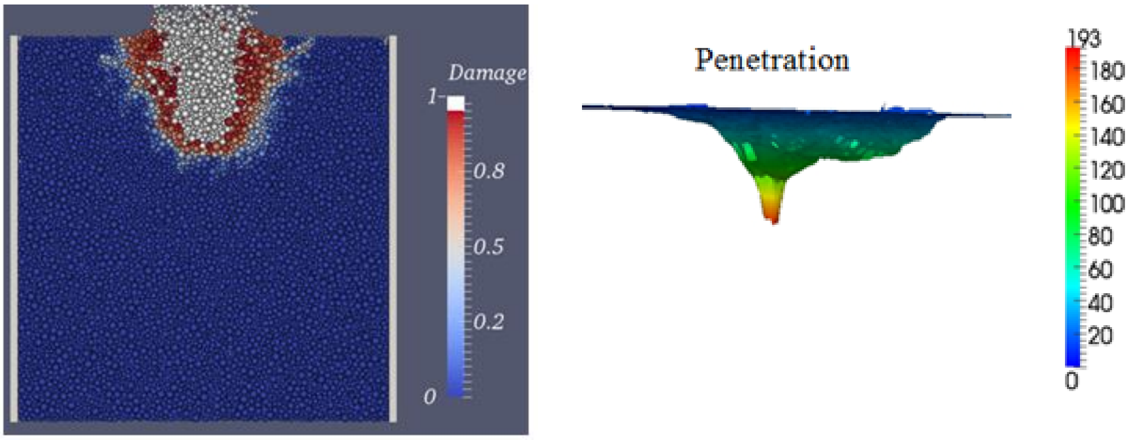

Figure 21. Penetration test at 227 m/s, crack pattern: simulation and experiment.

Figure 21 presents the crater observed in both the simulation and the experiment. The calculated penetration depth (193 mm) is the same as the measured one. The simulation accurately reproduces the observed phenomena, including spalling and cratering with conical cracks on the front face, as well as the size of the conical hole.

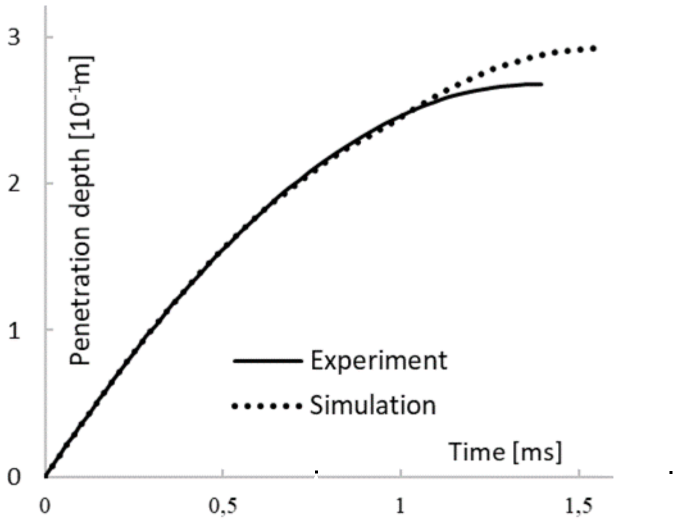

Figure 22. Penetration test at 347 m/s, simulation and experiment: projectile axial displacement

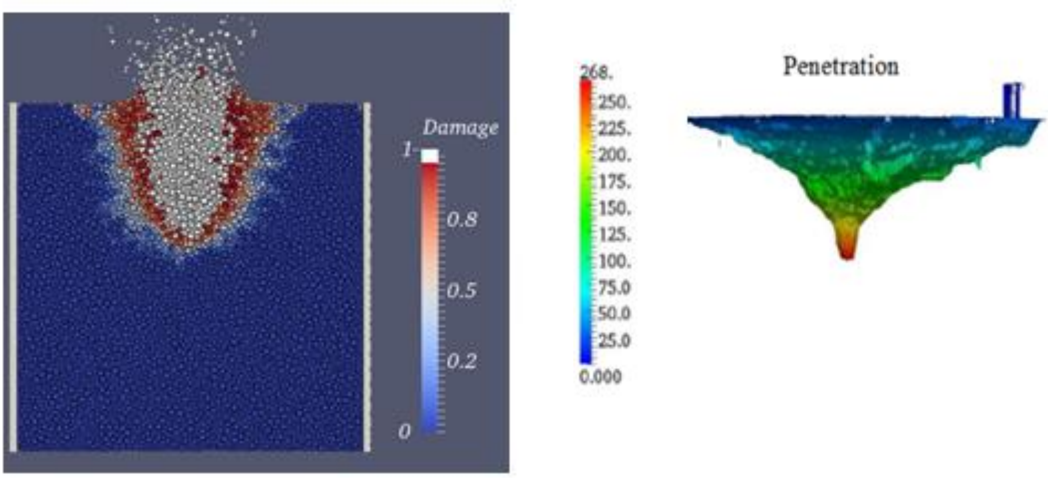

Figure 23. Penetration test at 347 m/s, crack pattern: simulation and experiment.

Figure 22 depicts the axial displacement of the projectile during the penetration test at 347 m/s. Compared to the test at 227 m/s, a more pronounced difference is observed after 1 ms. Figure 23 illustrates the crack pattern observed in both the simulation and the experiment. The calculated penetration depth (300 mm) is close to the measured one (268 mm). The damage pattern is realistically reproduced by the simulation, with spalling on the front face and the cratering damage mode, as well as tunneling through penetration.

Discussion

Bian et al. [55] presented FE simulations of the two penetration tests performed by CEA (one of the co-authors has performed the experiments and provided us the data). Bian et al. could correctly predict the penetration depths thanks to an erosion criterion based on the equivalent plastic deformation. To fit the experimental results, Bian et al. used a maximum equivalent plastic deformation equal to 200%. Such a value has no physical sense.

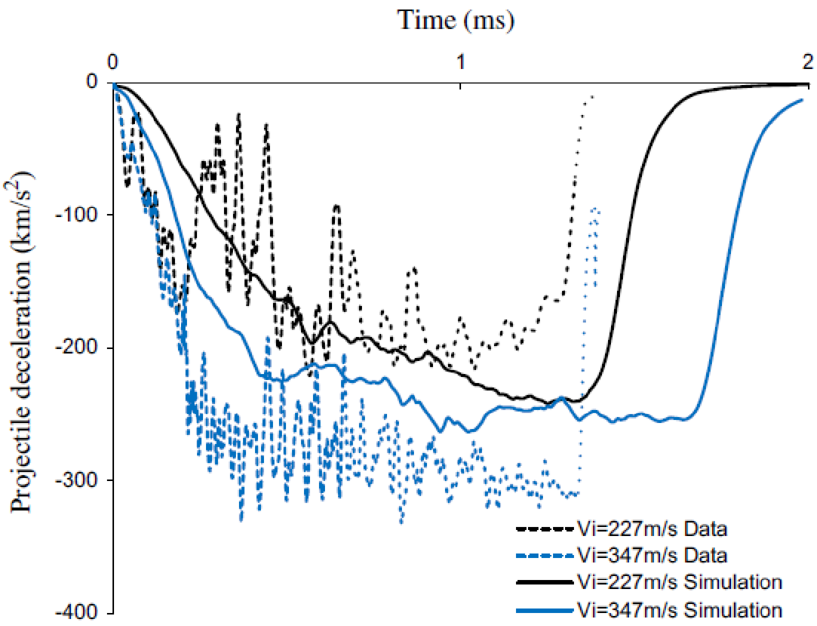

Figure 24. Penetration tests at 227 m/s and 347 m/s, projectile deceleration: experimental data and numerical results obtained by Bian et al. [55].

Nevertheless, an important scatter is observed between the numerical and the experimental projectile decelerations in the two penetration tests, especially after 1.4 ms (Figure 24). Analysis of the experimental signals seems to show a recording problem after 1.4 ms. The 347 m/s test generates greater inertia forces and therefore greater deceleration, which is observed. However, at 1.4 m/s the recorded accelerations drop to zero for both tests without explanation for that simultaneity. For this reason, the author of the tests informed us that the velocities and displacements calculated after 1.4 m/s might contain errors and should be considered with caution.

Conclusions

This article presents an extension of a DEM model implemented in Europlexus for the modeling of concrete structures under impulsive loading. The constitutive model for concrete is improved by integrating concrete compaction and identifying the tensile strength enhancement under high strain rates. Calibration of DEM parameters is conducted using an ordinary concrete, referencing laboratory tests including QS tension and compression, as well as QS confined compression and dynamic tensile tests.

Perforation and penetration tests performed by CEA on ordinary concrete targets confined with steel jackets were simulated with DEM. Concrete specimens were saturated with water for well-controlled curing conditions. Without fitting any parameter such an erosion criterion, calculated axial displacements of projectiles closely match the recorded ones during tests. The DEM model accurately reproduces damage patterns observed experimentally, such as spalling on the front side with an ejection of fragments and tunneling. Additionally, the simulation predicts the scabbing phenomenon with diagonal cracks developed on the rear face of the perforation specimen. A cratering damage mode is also observed in penetration simulations.

Impact tests on confined concrete targets validate the proposed compaction law, facilitating the study of concrete under high mean stresses due to impact. Furthermore, the reliability of the strain-rate effect modeling in tension is confirmed.

These results indicate that the current DEM approach, after years of development, has evolved into a robust computational tool. It effectively demonstrates the capacity to conduct realistic simulations within an industrial setting, particularly for concrete shields exposed to extreme dynamic loading scenarios.

Funding This research received support from Univ. Grenoble Alpes to fund the PhD grant of the first author; this research received funding from Electricité de France company and from CEA.

Data Availability The data presented in this study are available on request from the corresponding author.

Conflicts of Interest: The authors declare no conflict of interest.

Acknowledgments: Christophe Pontiroli from CEA is acknowledged for providing data and advice for the perforation and penetration tests.

References

1. Riera JD (1968) On the stress analysis of structures subjected to aircraft impact forces. Nucl Eng and Design, 8(4), 415-426

2. Kennedy RP (1976) A review of procedures for the analysis and design of concrete structures to resist missile impact effects. Nucl Eng and Design 37(2), 183-203
3. Li QM, Reid SR, Wen HM, Telford AR (2005) Local impact effects of hard missiles on concrete targets. Int J Impact Eng 32(1-4), 224-284
4. Berriaud C, Sokolovsky A, Gueraud R, Dulac J, Labrot R (1978) Comportement local des enceintes en beton sous l'impact d'un projectile rigide: Local behaviour of reinforced concrete walls under missile impact. Nucl Eng and Design 45(2), 457-469
5. Gran JK, Frew DJ (1997) In-target radial stress measurements from penetration experiments into concrete by ogive-nose steel projectiles. Int J Impact Eng 19(8), 715-726
6. Daudeville L, Malécot Y (2011) Concrete structures under impact. Eur J Environmental and Civil Eng 15, S1, 101-140
7. Bischoff PH, Perry SH (1991) Compressive behaviour of concrete at high strain rates. Mat and Struc 24(6), 425-450
8. Malvar LJ, Ross CA (1998) Review of strain rate effects for concrete in tension. ACI Mat J 95, 735-739
9. CEB (1988) Concrete structures under impact and impulsive loading. Lausanne,Switzerland: Comité Euro-International du Béton, Bulletin d'Information, 87
10. Rossi P, Van Mier JG, Boulay C, Le Maou F (1992) The dynamic behaviour of concrete: influence of free water. Mat and Struc 25(9), 509-514
11. Gatuingt F, Snozzi L, Molinari JF (2013) Numerical determination of the tensile response and the dissipated fracture energy of concrete: role of the mesostructure and influence of the loading rate. Int J for Numerical Analytical Methods in Geomech 37(18), 3112-3130
12. Weerheijm J, Forquin P (2013) Response mechanisms of concrete under impulsive tensile loading. In: Understanding the Tensile Properties of Concrete, 181-217, Woodhead Publishing
13. Schuler H, Mayrhofer C, Thoma K (2006) Spall experiments for the measurement of the tensile strength and fracture energy of concrete at high strain rates. Int J Impact Eng 32(10), 1635-1650
14. Cusatis G (2011) Strain-rate effects on concrete behavior. Int J Impact Eng 38(4), 162-170
15. Ruiyuan H, Zhenhuang G, Jian Q, Yanbo W, Zhichao L (2024) Strain rate effect of concrete based on split Hopkinson pressure bar (SHPB) test. J Building Eng 86, 108856

16. Zhang M, Wu HJ, Li QM, Huang FL (2009) Further investigation on the dynamic compressive strength enhancement of concrete-like materials based on split Hopkinson pressure bar tests. Part I: Experiments. Int J Impact Eng 36(12), 1327-1334
17. Zhou XQ, Hao H (2008) Modelling of compressive behaviour of concrete-like materials at high strain rate. Int J Sol and Struc 45(17), 4648-4661
18. Brace WF, Jones AH (1971) Comparison of uniaxial deformation in shock and static loading of three rocks. J Geophys Res, 76(20), 4913-4921
19. Piotrowska E, Forquin P, Malecot Y (2016) Experimental study of static and dynamic behavior of concrete under high confinement: Effect of coarse aggregate strength. Mech Mat 92, 164-174
20. Gabet T, Malécot Y, Daudeville L (2008) Triaxial behaviour of concrete under high stresses: Influence of the loading path on compaction and limit states. Cement Concrete Res 38(3), 403-412
21. Vu XH, Malecot Y, Daudeville L (2009) Strain measurements on porous concrete samples for triaxial compression and extension tests under very high confinement. J Strain Anal for Eng Design, 44(8), 633-657
22. Vu XH, Malecot Y, Daudeville L, Buzaud E (2009) Effect of the water/cement ratio on concrete behavior under extreme loading. Int J for Numerical Analytical Methods in Geomech 33(17), 1867-1888
23. Vu XH, Malecot Y, Daudeville L, Buzaud E (2009) Experimental analysis of concrete behavior under high confinement: Effect of the saturation ratio. Int J Sol Struc 46(5), 1105-1120
24. Vu XH, Daudeville L, Malecot Y (2011) Effect of coarse aggregate size and cement paste volume on concrete behavior under high triaxial compression loading. Constr Bldg Mat 25(10), 3941-3949
25. Vu XD, Briffaut M, Malecot Y, Daudeville L, Ciree B (2015) Influence of the saturation ratio on concrete behavior under triaxial compressive loading. Science Technology Nuclear Installations 2015(1), 976387
26. Cundall PA (1978) BALL–A Computer program to model granular media using the distinct element method. Technical Note TNLN-13, Advance Technology Group, Dames and Moore, London, 129-163
27. Cundall PA, Strack OD (1979) A discrete numerical model for granular assemblies. Geotechnique 29(1), 47-65

28. Cusatis G, Bažant ZP, Cedolin L (2003) Confinement-shear lattice model for concrete damage in tension and compression: I. Theory. J Eng Mech 129(12), 1439-1448
29. Donzé FV, Magnier SA, Daudeville L, Mariotti C, Davenne L (1999) Numerical study of compressive behavior of concrete at high strain rates. Eng Mech 125(10), 1154-1163
30. Hentz S, Daudeville L, Donzé FV (2004) Identification and validation of a discrete element model for concrete. J Eng Mech, 130(6), 709-719
31. Frangin E, Marin P, Daudeville L (2006) On the use of combined finite/discrete element method for impacted concrete structures. J Physique IV 134, 461-466
32. Rousseau J, Frangin E, Marin P, Daudeville L (2009) Multidomain finite and discrete elements method for impact analysis of a concrete structure. Eng Struct 31(11), 2735-2743
33. Rousseau J, Frangin E, Marin P, Daudeville L (2008) Damage prediction in the vicinity of an impact on a concrete structure: a combined FEM/DEM approach. Comp Concrete 5(4), 343-358
34. Shiu W, Donzé FV, Daudeville L (2008) Penetration prediction of missiles with different nose shapes by the discrete element numerical approach. Comp Struc 86(21-22), 2079-2086
35. Omar A, Marin P, Potapov S, Daudeville L (2013) 3D discrete element modeling of concrete: study of the rolling resistance effects on the macroscopic constitutive behavior. In Computational Plasticity XII: Fundamentals And Applications, Proceedings of the 12th International Conference on Computational Plasticity (COMPLAS) Ed by Onate E, Owen DRJ, D Peric, B Suarez, 575-586
36. Potapov S, Masurel A, Marin P, Daudeville L (2017) Mixed DEM/FEM modeling of advanced damage in reinforced concrete structures. J Eng Mech 143(2), 04016110
37. Antoniou A (2018) Discrete element modelling of concrete structures under impact. PhD thesis, Univ Grenoble Alpes, Grenoble, France
38. Daudeville L, Antoniou A, Marin P, Forquin P, Potapov S (2022) Discrete element approach to model advanced damage in concrete structures under impact. In Handbook of Damage Mechanics: Nano to Macro Scale for Materials and Structures, Cham: Springer International Publishing, 517-550
39. Europlexus, A computer program for analysis of fast transient phenomena involving structures and fluids in interaction, http://www-epx.cea.fr (accessed on April 10 2024)
40. Salome, Computer software, http://www.salome-platform.org (accessed on 10 April 2024)
41. Cui L, O'Sullivan C (2003) Analysis of a triangulation based approach for specimen generation for discrete element simulations. Granular Matter 5(3), 135-145

42. Jerier JF, Imbault D, Donzé FV, Doremus P (2009) A geometric algorithm based on tetrahedral meshes to generate a dense polydisperse sphere packing. Granular Matter 11(1), 43-52
43. Herrmann HJ, Hansen A, Roux S (1989) Fracture of disordered, elastic lattices in two dimensions. Phys Review B 1989, 39(1), 637-647
44. Cambou, B, Dubujet, P, Emeriault, F, Sidoroff, F (1995) Homogenization for granular materials. Eur J Mech A Solids 1995, 14(2), 255-276
45. Liao CL, Chang TP, Young DH, Chang CS (1997) Stress-strain relationship for granular materials based on the hypothesis of best fit. Int J Sol Struc, 34(31-32), 4087-4100
46. Omar, A, Marin, P, Potapov, S, Daudeville, L (2013) 3D discrete element modeling of concrete: Study of the rolling resistance effects on the macroscopic constitutive behavior. In Proceedings of the XII International Conference on Computational Plasticity: fundamentals and applications, Barcelona, Spain, 3-5 Sept, 575-586
47. Burton P (1961) A modification of the Coulomb-Mohr theory of fracture. J Applied Mech, 28(2), 259-268
48. Malecot Y, Daudeville L, Dupray F, Poinard C, Buzaud E (2010) Strength and damage of concrete under high triaxial loading. Eur J Environmental Civil Eng 2010, 14(6-7), 777-803
49. Shiu W, Donzé FV, Daudeville L (2008) Compaction process in concrete during missile impact: a DEM analysis. Comp Concrete 5(4), 329-342
50. Benniou H, Accary A, Malecot Y, Briffaut M, Daudeville L (2021) Discrete element modeling of concrete under high stress level: influence of saturation ratio. Comp Particle Mech 8, 157-167
51. Accary A, Malecot Y, Daudeville L (2019) Design and evaluation of a deformable sensor for interstitial pore pressure measurement in concrete under very high stress level. Appl Sc 9(13), 2610
52. Erzar B, Forquin P (2014) Analysis and modelling of the cohesion strength of concrete at high strain-rates. Int J Sol Struc 51(14), 2559-2574
53. Novikov SA, Divnov II, Ivanov AG (1966) Failure of steel, aluminium and copper under explosive shock loading. Phys Metals Metallogr 21(4), 122-128
54. Forquin P, Erzar B (2010) Dynamic fragmentation process in concrete under impact and spalling tests. Int J Frac 163(1-2), 93-215
55. Brian H, Jia Y, Shao J, Pontiroli C (2016) Numerical study of a concrete target under the penetration of rigid projectile using an elastoplastic damage model. Eng Struc 111, 525-537